

# Study of Wirelessly Accessible Planar Mirrored-Coil Sensor and its Resonant Frequency in Bio-medicine

Jonghun Lee, Hyunwoo Kim, Kunwoo Park, Jong-Han Kim,<sup>\*</sup> and Sanghoek Kim <sup>‡</sup>  
*Electronic Engineering Department, Kyung Hee University, Yongin-si, South Korea <sup>†</sup>*

Rehab S. Hassan  
*Biomedical Engineering Department, Kyung Hee University, Yongin-si, South Korea*  
 (Dated: January 28, 2021)

Planar mirrored-coil sensors are widely used in the field of bio-medicine to measure physiological signals. Although, there are many studies on interrogation methodologies, research on the sensor itself remains understudied. Here we report an analytical formulation and a data-fitted closed form formula to calculate the resonant frequency for a planar mirrored-coil sensors. Compared to field solvers, our analytical formula and closed-form formula results in 11 % and 9% median errors respectfully. Since closed-form formulas are computationally efficient, it offers a way for designing and optimizing planar mirrored-coil sensors.

## I. INTRODUCTION

LC-resonator based sensors are widely used to sense physiological signals, such as pressure, for various diagnosis and health monitoring purposes. The examples that sense pressure are blood pressure [1], intracranial pressure[2], intraocular pressure [3–6], bladder pressure[7]. To sense pressure, most studies utilize the principle that the capacitance formed between two mirrored coils increases as the separation between the coils decreases when the external pressure is applied. The increase of capacitance subsequently lowers down the resonant frequency of the sensor  $\omega_s$  which is formed between the capacitance and the inherent inductance of the coil.

The key benefit of LC-based pressure sensor compared to other types of pressure sensor, such as resistive sensor [8], lies in the easiness of wireless accessibility from outside the body. While the resistive sensor requires a complicated readout system, including analog-to-digital converter and a separate communication module, to obtain the sensed value wirelessly, the LC-based sensor inherently provides the wireless accessibility to the resonant frequency through the inductive coupling with an external interrogator.

Among various LC-resonator structures, mirrored-coil structures are a compelling candidate since they can be fabricated as small as  $1 \times 1 \text{ mm}$ . This is because mirrored-coil structures do not require a via [2] which hinders miniaturization due to its large footprint. Also, it requires additional fabrication steps which increases the overall cost.

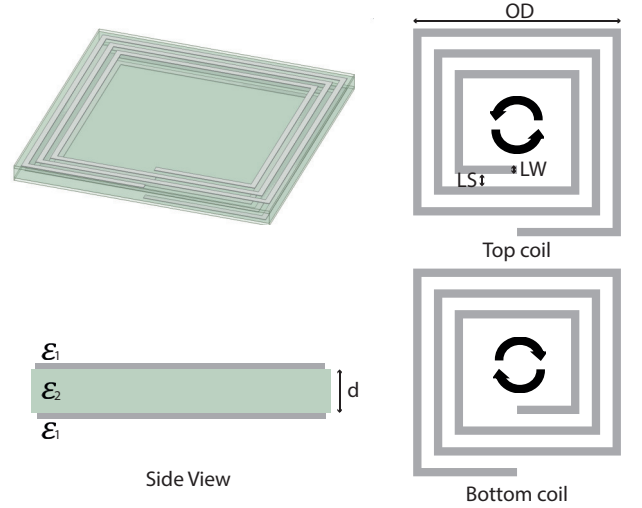


FIG. 1. Structure of a mirrored coil LC sensor. The top coil and bottom coil rotate in different directions.

There are many ways to access the resonant frequency from the interrogator. A traditional, but still the most popular method is to place the external interrogator of which the resonant frequency  $\omega_1$  is much higher than that of the sensor. When the electromagnetic energy with the frequency varying near  $\omega_s$  excites the interrogator, where the amount of the energy emanating from the interrogator is assumed constant with frequency since  $\omega_1 \gg \omega_s$ , a part of the energy is inductively coupled into the sensor. The interrogator identifies the resonant frequency at which the electromagnetic energy is absorbed particularly well by the resonance at the sensor. A drawback of this approach, however, is that the sensitivity and the sensing resolution is severely degraded when Q-factor of the sensor is low and the coupling strength  $\kappa$  between the interrogator and the sensor is weak. To overcome this limitation and improve the sensing capabilities, [9] has proposed the idea of  $\mathcal{PTX}$ -symmetric telemetry, at which a scale-transformed( $\mathcal{X}$ ) interrogator having the same res-

<sup>\*</sup> <sup>‡</sup> Authors to whom correspondence should be addressed: Sanghoek Kim (sanghoek@khu.ac.kr) and Jong-Han Kim (jonghank@khu.ac.kr)

<sup>†</sup> Also at Electronics and Information Convergence Engineering Department, Kyung Hee University, Yongin-si, South Korea ; Institute of Wearable Convergence Electronics, Kyung Hee University, Yongin-si, South Korea

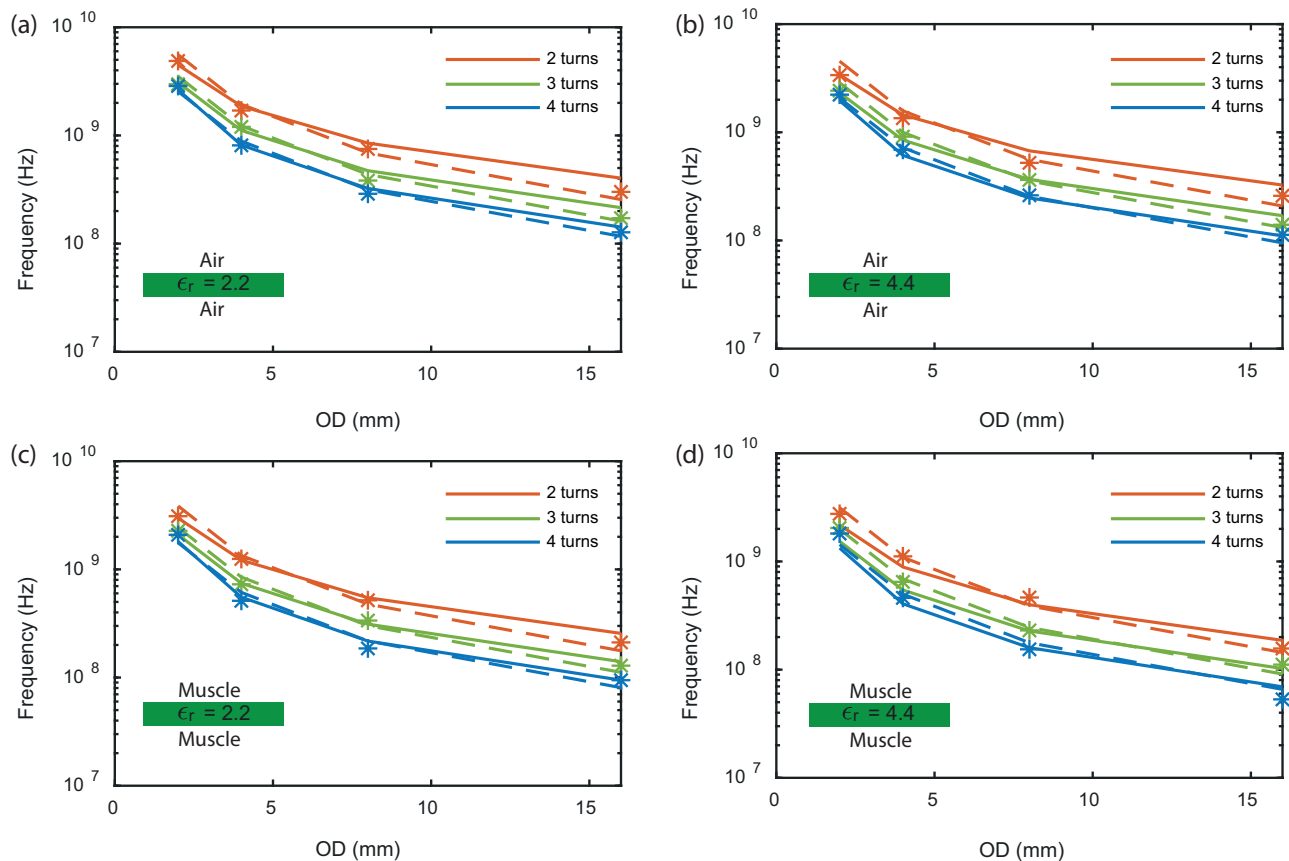


FIG. 2. Plot of resonant frequency for various coil parameters. Solid line indicates analytical calculations, dashed line indicates calculations using closed-form formula and markers represent results from FEM. The parameters for each subplot are as follows. (a)  $\epsilon_r = 2.2$ , in air. (b)  $\epsilon_r = 4.4$ , in air. (c)  $\epsilon_r = 2.2$ , in muscle. (d)  $\epsilon_r = 4.4$ , in muscle.

onant frequency  $\omega_1 = \omega_s$  with the sensor, sharpens the linewidth. This technique improves the sensing resolution and the overall sensitivity, but limited to use only when the coupling strength  $\kappa$  is strong enough. When the coupling strength  $\kappa$  is weak due to the depth and small dimension of the sensor, the interrogator consisting of two resonators locked to an exceptional point can react exotically well to the weakly coupled sensor, enabling highly sensitive readout [10].

While there have been intensive studies about how to wirelessly readout the resonant frequency of mirrored-coil sensor, the study of mirrored-coil sensor itself is poorly done relatively. To briefly review the analytical study related to passive sensor, the closed-form formula [11] for the inductance of a single planar coil is widely used to design both printed circuits and on-die inductors. Likewise, parasitic capacitance of a planar coil can be computed through conformal mapping [12, 13]. However, the capacitance formed between two planar coils is lack of studies for both analysis and optimization. As a result, investigators utilize the sensor with a primitive design without further optimization, resorting on the most basic equation of the capacitance between two parallel plates,  $C = \epsilon A/d$ , where  $A$  and  $d$  refer the plate area and the sep-

aration between the plates, respectively. The prediction of the formula about the tendency between the capacitance and the separation is still valid, but the precision cannot be good since the coil structure is not a plate at all. The stray capacitance between the trace and the fringing field should be considered to be precise. There also have been attempts to calculate the resonant frequency of two split-ring resonators (SRR dimers) using coupled-mode theory (CMT)[14]. However, the calculation process is semi-analytical, which means that the calculation relies on preliminary field data computed from commercial field solvers.

This work presents an analytical tool and a closed-form formula about the resonant frequency of mirrored-coil sensor of a specific shape.

## II. CALCULATION OF THE LC-RESONANT FREQUENCY

From electromagnetic theory, an effective inductance  $L$  and an effective capacitance  $C$  for a closed system can

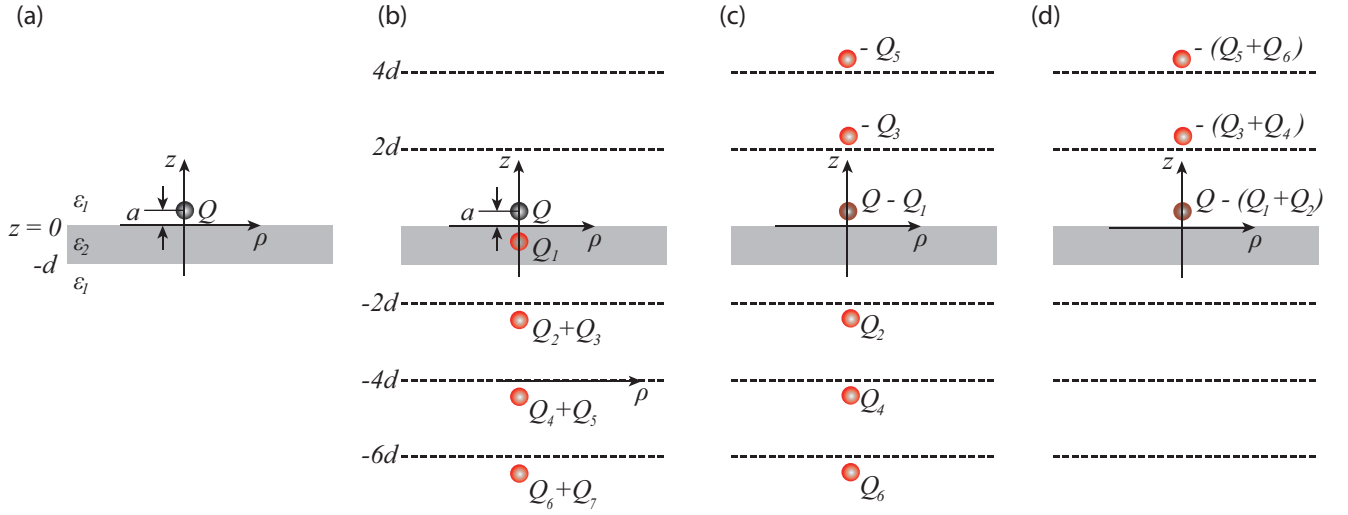


FIG. 3. Distribution of image charges to satisfy the boundary condition at  $z = 0$  and  $z = -d$ . (a) Location of the unit charge. (b) Distribution of image charges for  $z > 0$ . (c) Distribution of image charges for  $-d < z < 0$ . (d) Distribution of image charges for  $z < -d$ .

be defined as follows:

$$L = \frac{1}{|I_0|^2} \iint d\mathbf{r} d\mathbf{r}' \mathbf{J}(\mathbf{r}) \cdot \bar{\mathbf{G}}_{\mathbf{A}}(\mathbf{r}, \mathbf{r}') \mathbf{J}(\mathbf{r}') \quad (1)$$

$$\frac{1}{C} = \frac{1}{|q_0|^2} \iint d\mathbf{r} d\mathbf{r}' \rho(\mathbf{r}) G_V(\mathbf{r}, \mathbf{r}') \rho(\mathbf{r}') \quad (2)$$

where  $\bar{\mathbf{G}}_{\mathbf{A}}$  ( $G_V$ ) refers the Green's operator on current (charge) density for the vector (scalar) potential  $\mathbf{A}$  ( $V$ ).  $I_0$  and  $q_0$  are the reference current and the reference charge. At resonance, the current profile  $\mathbf{J}$  and the charge profile  $\rho$  on a coil structure are well approximated by the sinusoidal function at its lowest mode[15]. With this approximation, the charge conservation law  $\nabla \cdot \mathbf{J} = -\frac{\partial \rho}{\partial t}$  relates the reference current profile and the charge profile as  $|I_0| = 2\pi f |q_0|$ , where  $f$  is the operating frequency.

It is noteworthy to mention that the mirrored layout creates opposite charges at the end of the top and bottom inductors. This opposite charge creates higher capacitance than the case which the top and bottom inductors are rotating in the same directions.

Lastly, as defined, the resonant frequency is the frequency at which the average amount of the magnetic energy  $L|I_0|^2/2$  and the electric energy  $C|q_0|^2/2$  are equal. This yields the well-known equation of the resonant frequency:

$$f_0 = \frac{1}{2\pi\sqrt{LC}} \quad (3)$$

#### A. LC resonator in homogeneous media

In a homogeneous medium of permittivity  $\epsilon$  and a permeability  $\mu$ , the Green's operators for potentials act on

the operands as

$$\bar{\mathbf{G}}_{\mathbf{A}}(\mathbf{r}, \mathbf{r}') \mathbf{J}(\mathbf{r}') = \frac{\mu}{4\pi} \frac{\mathbf{J}(\mathbf{r}')}{|\mathbf{r} - \mathbf{r}'|} \quad (4)$$

$$G_V(\mathbf{r}, \mathbf{r}') \rho(\mathbf{r}') = \frac{1}{4\pi\epsilon} \frac{\rho(\mathbf{r}')}{|\mathbf{r} - \mathbf{r}'|} \quad (5)$$

resulting the potentials from Biot-Savart's law and Coulomb's law, respectively. Although these simple operators are widely used for wireless antenna applications, they cannot analyze the resonating property of a sensor composed of heterogeneous media, such as a biomedical sensor of which the substrate typically has a different electrical properties from the surrounding tissue medium. The Green's operators need to be modified to accommodate the in-homogeneity of media.

#### B. LC resonator in in-homogeneously layered media

Since human body and most substrates on which the sensor is fabricated is non-magnetic, the inductance  $L$  of the coil sensor can still be obtained from (1) and (4) or from empirical findings [11]. In contrast, the permittivity largely differs between substrate and tissues, which necessitates the modification of (5) in (2).

Modeling the substrate in a medium as a planarly layered media as in Fig. 3(a), the Green's operator for the electric potential can be derived by the method of images [16]. The method of images can be applied to solve the fields in the presence of slab of  $\epsilon_2$  as in Fig. 3(a). The boundary conditions are imposed at both interfaces

of  $z = 0$  and  $z = -d$ . Specifically,

$$\begin{aligned}\epsilon_1 E_{1,n} &= \epsilon_2 E_{2,n} \\ E_{1,t} &= E_{2,t} \\ \epsilon_2 E_{2,n} &= \epsilon_1 E_{3,n} \\ E_{2,t} &= E_{3,t}\end{aligned}$$

The numerical indexes in the subscripts refer the fields in the region 1 ( $z > 0$ ), the region 2 ( $0 > z > -d$ ), and the region 3 ( $z < -d$ ).

To satisfy the boundary condition, infinite number of image charges are required. To represent the field and potential in the region 1, it can be shown that the image charges should be positioned as in Fig. 3(b), while for the fields and potentials in the region 2 and 3, the image charges should locate as in Fig. 3(c) and (d). When  $z_n^m$  denotes the  $z$  coordinate of charge  $n$ -th image charge  $Q_n$  for the potential in the region  $m$ , the first few of  $z_n^m$  are listed as below:

$$\begin{aligned}z_1^1 &= -a \\ z_2^1 &= z_3^1 = -2d - a \\ z_4^1 &= z_5^1 = -4d - a, \dots \\ z_1^2 &= +a \\ z_2^2 &= -2d - a \\ z_3^2 &= 2d + a, \dots \\ z_1^3 &= z_2^3 = +a \\ z_3^3 &= z_4^3 = 2d + a \\ z_5^3 &= z_6^3 = 4d + a, \dots\end{aligned}$$

The values of image charge  $Q_n$  can be determined by enforcing the boundary condition. For the purpose of reference, the values of image charge  $Q_n$  and their corresponding location  $z_n^m$  in  $z$ -coordinate are as follows:

$$Q_1 = \frac{\epsilon_1 - \epsilon_2}{\epsilon_1 + \epsilon_2} Q \quad (6)$$

$$Q_2 = \frac{2\epsilon_2}{\epsilon_1 + \epsilon_2} Q \quad (7)$$

$$Q_n = (-1)^{n-1} \frac{\epsilon_1 - \epsilon_2}{\epsilon_1 + \epsilon_2} Q_{n-1}, (n = 3, 4, 5 \dots) \quad (8)$$

To solve the electric potential by the unit charge  $Q$ , the distribution of image charges can be chosen depending on the region of interests. For example, the potential in the region 1 ( $z > 0$ ) by the charge  $Q$  at  $\mathbf{r}'$  (where  $z' > 0$ ) can be expressed as

$$\begin{aligned}V(\mathbf{r}; Q \text{ at } \mathbf{r}') \\ = \frac{1}{4\pi\epsilon_1} \left[ \frac{Q}{\sqrt{\rho^2 + (z-a)^2}} + \sum_{n=1}^{\infty} \frac{Q_n}{\sqrt{\rho^2 + (z-z_n^1)^2}} \right]\end{aligned}$$

By definition, the Green's operator for the electric potential  $V$  is  $G_V(\mathbf{r}, \mathbf{r}') = V(\mathbf{r}; Q \text{ at } \mathbf{r}')/Q$ . For planar coils,

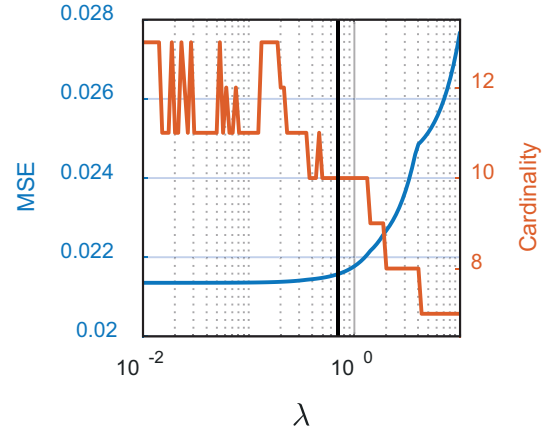


FIG. 4. Regularization path for optimal MSE and the cardinality of the predictor parameter.

all the charges locate on the surfaces of the substrate. From the continuity of electric potential, we selected the distribution of image charges for the region 2 to obtain  $G_V(\mathbf{r}, \mathbf{r}')$  of interests.

$$\begin{aligned}G_V(\mathbf{r}, \mathbf{r}') \\ = \frac{1}{4\pi\epsilon_2} \left[ \frac{1}{|\mathbf{r} - \mathbf{r}'|} + \sum_{n=1}^{\infty} \frac{\alpha_n}{|\mathbf{r} - \mathbf{r}'_n|} \right]\end{aligned}$$

where  $\alpha_n$  and  $\mathbf{r}'_n$  indicate the magnitude and the position of  $n$ -th image charge.

### C. Closed-Form Formula

Analytical calculations provide physical insight into how the LC-sensor behaves at resonance. However, for practical purposes, it is feasible to have a closed-form formula to calculate the resonant frequency. This is because, closed-form formulas require only a few lines of code for implementation. Also, it is computationally efficient than analytical calculations or field solvers.

In this section, we build an empirical closed-form formula for the resonance frequency of planar mirrored-coil sensors. We collected 1,070 data samples from the HFSS computation results, among which 603 ( $= n_{\text{train}}$ ) samples are used for training and the rest for validation. The samples have 6 input features,  $x_1, \dots, x_6$ , which are scaled by their maximum range in the training data set, so that they do not exceed one.

- $x_1$ : number of turns, scaled by 4
- $x_2$ : surface permittivity, scaled by 50
- $x_3$ : LS over LW, scaled by 0.3

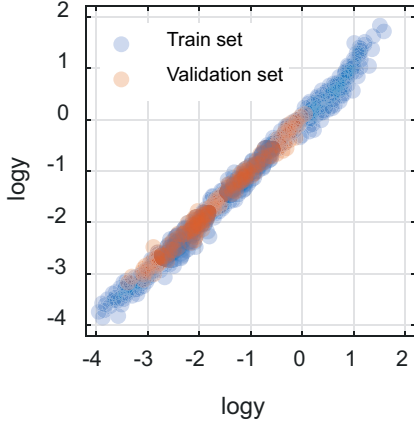


FIG. 5. Prediction accuracy of the empirical model,  $\log \hat{y}$  vs.  $\log y$ .

- $x_4$ : distance between the plates in mm, scaled by 0.6
- $x_5$ : permittivity of surrounding material, scaled by 8
- $x_6$ : outer diameter in mm, scaled by 32

The output feature of the samples,  $y$ , is the resonant frequency, which we assume to be related by the product of a monomial function and exponential functions of the input features. This leads to the following prediction model,

$$\hat{y} = e^b \prod_{i=1}^6 x_i^{\theta_i} e^{\beta_i x_i}$$

where  $\hat{y}$  is the predicted resonant frequency and  $b, \theta_1, \beta_1, \dots, \theta_6, \beta_6$  are the predictor parameters that we will find. Taking the logarithm and denoting the sample number in the superscript with the parentheses gives,

$$\log \hat{y}^{(k)} = b + \sum_{i=1}^6 \left( \theta_i \log x_i^{(k)} + \beta_i x_i^{(k)} \right)$$

which implies that the logarithm of the predicted frequency is linear in the predictor parameters.

Now we define the following loss function describing the model fitness over the train set,

$$\mathcal{L}(b, \theta_1, \beta_1, \dots, \theta_6, \beta_6) = \sum_{k=1}^{n_{\text{train}}} \left( \log \hat{y}^{(k)} - \log y^{(k)} \right)^2$$

with the  $\ell_1$  regularizer promoting sparsity in the predictor parameters,

$$r(\theta_1, \beta_1, \dots, \theta_6, \beta_6) = \sum_{i=1}^6 (|\theta_i| + |\beta_i|)$$

Then we find the optimal predictor parameters fitting the train set by solving the following LASSO (Least absolute shrinkage and selection operator) type problem [17]

TABLE I. MSE and percentage error of the empirical model.

	MSE	RMSE	Percentage error
Train set	0.02157	0.1469	15.8%
Validation set	0.01354	0.1164	12.3%

with a nonnegative weighting parameter  $\lambda$ ,

$$\underset{b, \theta_1, \beta_1, \dots}{\text{minimize}} \quad \mathcal{L}(b, \theta_1, \beta_1, \dots) + \lambda r(\theta_1, \beta_1, \dots)$$

Note that this can be easily solved by general off-the-shelf convex optimization solvers, such as `cvxpy`[18].

Figure 4 shows the optimal  $\text{MSE} = \mathcal{L}^*/n_{\text{train}}$  and the cardinality of  $b, \theta_1, \beta_1, \dots, \theta_6, \beta_6$  for  $0.01 \leq \lambda \leq 10$ . From this regularization path, we choose  $\lambda = 0.7$  (the vertical black line) since it simplifies the model by sufficiently reducing the cardinality while increasing the MSE no more than 2% from its attainable minimum. We present below the empirical formula obtained from  $\lambda = 0.7$ :

$$\hat{y} = 0.02490 \frac{1.069 x_2^{0.8181} x_5^{1.399} x_6^{0.2260} x_4^{0.1603}}{x_1^{1.131} x_2^{0.1110} x_5^{0.2165} x_6^{1.553}}$$

The prediction accuracy is assessed in Figure 5 and Table I. The prediction and the ground-truth resonant frequency from the data set are plotted in Figure 5, where the blue dots and the orange dots represent sample points from the train set and the validation set, respectively.

### III. COMPARISON TO FIELD SOLVERS

To validate our calculations in section II, we simulate mirrored coil LC sensors using a commercial finite element method (FEM) solver HFSS. An external reader is designed to have a 1 turn coil so that the resonant frequency is higher than the resonant frequency of the LC-sensor. Then the external reader is placed 5 mm above the LC resonator. The resonant frequency of the LC-sensor is determined by finding the maximum power reflection distortion (PRD)[2].

Figure 2 shows the analytical calculation results compared with results from FEM. The solid line (dashed line) indicates analytical calculation (closed-form formula) results whereas the marked indicates values obtained from FEM. The values are compared for various parameters when the line width and line spacing is fixed to 0.5 mm respectively. For all the parameters listed above, the results show a good agreement between analytical calculations and FEM results.

We next use the absolute percentage error to analyze the accuracy of analytical calculations. The absolute percentage error is obtained as  $100|f_{\text{calculation}} - f_{\text{FEM}}|/f_{\text{FEM}}$ . This corresponds to the x-axis of Figure 6(a). The y-axis of Figure 6(a) indicates the percentage of samples that exceed the specified absolute error.

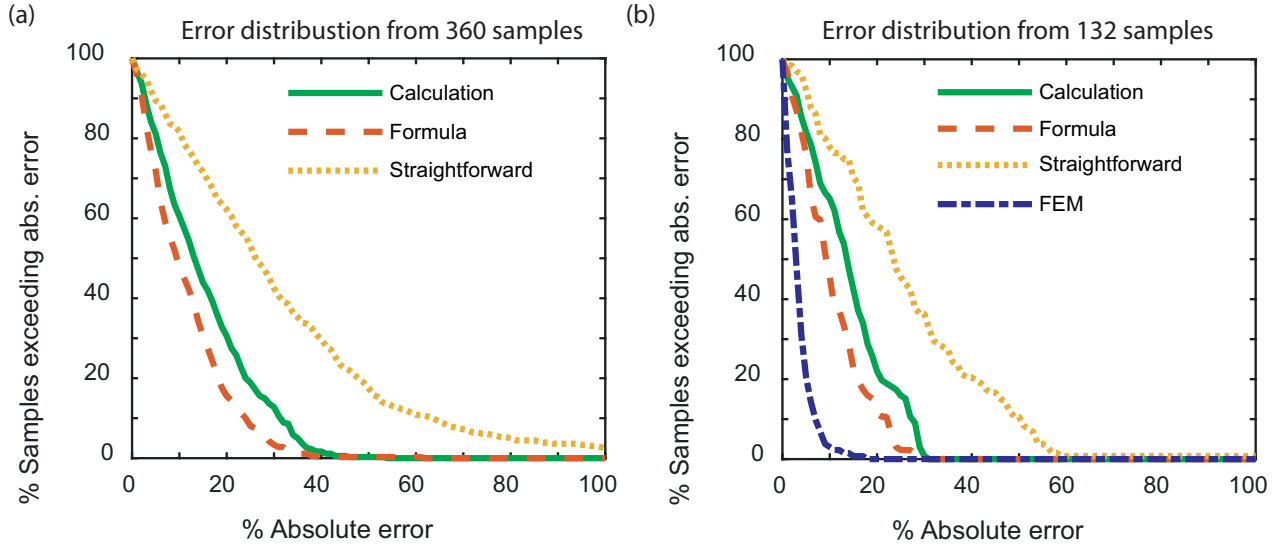


FIG. 6. Error distributions for (a) analytical calculations (solid), closed-form formula calculations (dash) and straightforward calculations (dot) compared to field solvers, (b) analytical calculations (solid), closed-form formula calculations (dash), straightforward calculations (dot) and FEM simulations (dash dot) compared to measurement results .

Figure 6(a) shows the error distributions of analytical calculation, closed-form formula calculation and straight forward calculation results compared to FEM simulation results. The straight forward calculation is obtained simply by calculating the capacitance as  $C = \epsilon_2 \frac{A}{d}$  where  $A$  is the intersecting area between the top and bottom coils. The error distribution is obtained from 360 samples where the number of turns is varied between 2 to 4, outer diameter is varied between 2 mm to 8 mm, relative permittivity is varied between 2.2 to 8.8, relative permittivity of the surrounding material is varied between 1 to 50 and finally, the line width and line spacing is varied between 0.1 mm to 0.3 mm respectively. These values are selected based on dimensions of LC-sensors for implantable purposes.

The median error is obtained by following the horizontal line at the 50% level[11]. Figure 6(a) shows that the median error for analytical calculations and closed-form formula is around 13% and 9% respectively which is significantly smaller than the straightforward calculations which has a median error of 26%.

#### IV. MEASUREMENT RESULTS

We fabricate LC-sensors on an FR-4 board using standard PCB technology and measure the resonant frequency for 132 different parameters. A few of the parameters selected for measurement is shown in Table II and the rest is provided in the supplementary material. The measurement is performed in air, fresh water and ethanol-water mixture to mimic the permittivity to the human muscle in the microwave regime. 4 spacers are placed at the corners of the FR-4 board so that the

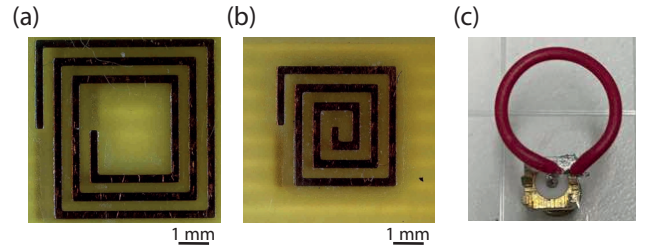


FIG. 7. Fabricated LC-sensor, (a) with a 6 mm diameter and (b) a 4 mm diameter. (c) External reader for measurement

external material completely surrounds the LC-sensor. Then a single coil reader with a radius of 7 mm is placed above the LC-sensor as shown in Fig 7(c). The resonant frequency is determined by using the aforementioned method from section III based on results exported from a vector network analyzer (Rohde & Schwarz ZNLE6).

Figure 6(b) shows the error distribution of analytical, closed-form formula, straight forward calculations and FEM simulation results. The error distribution was obtained by calculating the absolute percentage error as  $100|f_{\text{calculation}} - f_{\text{measured}}|/f_{\text{measured}}$ . It showed that FEM simulations have the least error of less than 3% since it considers every detailed aspect of the mirrored-coil sensor. For instance, the thickness of the copper layer or the thin OSP (organic solderability preservative) layer that goes on top of the copper layer to prevent unwanted shorting effects. Then, the straightforward calculation results had the highest error of 23% since it does not consider any high-frequency behaviour of the LC sensor. Finally, analytical calculations and closed-form formula calculations resulted in a median error of 13% and 9% respectively which is smaller than straightforward calcu-



lations but higher than FEM simulations.

## V. CONCLUSIONS

In this work, we have offered two different methods for calculating the resonant frequency of planar mirrored-coil sensors in environments such as air or the human muscle. The first (analytical calculation) method is based on an assumption that the charge profile is well approximated by a sinusoidal function at the lowest mode. Then the corresponding current density can be obtained from the charge conservation law. By applying Green's operators to the source profiles, we obtain the effective inductance and capacitance which can be used to calculate the resonant frequency. Also the effect of the dielectric permittivity of the outside material and substrate is considered by applying the method of images. The second (closed-form formula) method is based on solving the LASSO type problem assuming that the resonant frequency is a product of a monomial function and exponential functions of the coil parameters.

For both methods, the calculation results agrees well

with results from a field-solver with a median error of 13 % (9 %) for analytical calculations (closed-form formulas). The results are also compared to measurement results where the median error results in 13 % (9 %) for analytical calculations (closed-form formulas).

The analytical calculation provides a comprehensive understanding of the operating mechanisms of planar mirrored-coil sensors. Closed-form formulas are computationally efficient and easy to implement. Therefore, we vision that closed-form formulas can be suitable for designing and optimizing planar mirrored-coil sensors

## ACKNOWLEDGMENT

This work was supported by the National Research Foundation of Korea (NRF) grant NRF-2017R1C1B2009892, NRF-2018R1A6A1A03025708, and MSIT (Ministry of Science and ICT), Korea, under the ITRC (Information Technology Research Center) support program (IITP-2016-0-00291- 0051001) supervised by the IITP (Institute for Information & communications Technology Planning & Evaluation).

- 
- [1] C. M. Boutry, L. Beker, Y. Kaizawa, C. Vassos, H. Tran, A. C. Hinckley, R. Pfattner, S. Niu, J. Li, J. Claverie, *et al.*, Biodegradable and flexible arterial-pulse sensor for the wireless monitoring of blood flow, *Nature biomedical engineering* **3**, 47 (2019).
  - [2] L. Y. Chen, B. C.-K. Tee, A. L. Chortos, G. Schwartz, V. Tse, D. J. Lipomi, H.-S. P. Wong, M. V. McConnell, and Z. Bao, Continuous wireless pressure monitoring and mapping with ultra-small passive sensors for health monitoring and critical care, *Nature communications* **5**, 1 (2014).
  - [3] G. Chitnis, T. Maleki, B. Samuels, L. B. Cantor, and B. Ziaie, A minimally invasive implantable wireless pressure sensor for continuous iop monitoring, *IEEE Transactions on Biomedical Engineering* **60**, 250 (2012).
  - [4] P.-J. Chen, D. C. Rodger, S. Saati, M. S. Humayun, and Y.-C. Tai, Microfabricated implantable parylene-based wireless passive intraocular pressure sensors, *Journal of Microelectromechanical Systems* **17**, 1342 (2008).
  - [5] P.-J. Chen, S. Saati, R. Varma, M. S. Humayun, and Y.-C. Tai, Wireless intraocular pressure sensing using microfabricated minimally invasive flexible-coiled lc sensor implant, *Journal of Microelectromechanical Systems* **19**, 721 (2010).
  - [6] S.-Y. Wu, C. Yang, W. Hsu, and L. Lin, 3d-printed microelectronics for integrated circuitry and passive wireless sensors, *Microsystems & Nanoengineering* **1**, 1 (2015).
  - [7] J. Melgaard, J. J. Struijk, and N. J. Rijkhoff, Minimizing a wireless passive lc-tank sensor to monitor bladder pressure: A simulation study, *Journal of medical and biological engineering* **37**, 800 (2017).
  - [8] A. D. Mickle, S. M. Won, K. N. Noh, J. Yoon, K. W. Meacham, Y. Xue, L. A. McIlvried, B. A. Copits, V. K. Samineni, K. E. Crawford, *et al.*, A wireless closed-loop system for optogenetic peripheral neuromodulation, *Nature* **565**, 361 (2019).
  - [9] P.-Y. Chen, M. Sakhdari, M. Hajizadegan, Q. Cui, M. M.-C. Cheng, R. El-Ganainy, and A. Alù, Generalized parity-time symmetry condition for enhanced sensor telemetry, *Nature Electronics* **1**, 297 (2018).
  - [10] Z. Dong, Z. Li, F. Yang, C.-W. Qiu, and J. S. Ho, Sensitive readout of implantable microsensors using a wireless system locked to an exceptional point, *Nature Electronics* **2**, 335 (2019).
  - [11] S. S. Mohan, M. del Mar Hershenson, S. P. Boyd, and T. H. Lee, Simple accurate expressions for planar spiral inductances, *IEEE Journal of solid-state circuits* **34**, 1419 (1999).
  - [12] X. Jin, Q. Wang, W. Q. Khan, Z. H. Tang, and X. M. Yao, Analytical computation of distributed capacitance for nfc coil antenna, *IEICE Electronics Express* **14**, 20161147 (2017).
  - [13] U.-M. Jow and M. Ghovanloo, Modeling and optimization of printed spiral coils in air, saline, and muscle tissue environments, *IEEE transactions on biomedical circuits and systems* **3**, 339 (2009).
  - [14] S. Y. Elnaggar, R. J. Tervo, and S. M. Mattar, Energy coupled mode theory for electromagnetic resonators, *IEEE Transactions on Microwave Theory and Techniques* **63**, 2115 (2015).
  - [15] A. Kurs, A. Karalis, R. Moffatt, J. D. Joannopoulos, P. Fisher, and M. Soljačić, Wireless power transfer via strongly coupled magnetic resonances, *science* **317**, 83 (2007).
  - [16] J. D. Jackson, *Classical electrodynamics* (John Wiley & Sons, 2007).
  - [17] T. Hastie, R. Tibshirani, and J. Friedman, *The elements of statistical learning: data mining, inference, and pre-*

TABLE II. Inductor parameters used for experiments and comparison to calculations and field solvers

N	$\epsilon_{r1}$	LW/LS (mm)	d (mm)	$\epsilon_{r2}$	OD (mm)	FEM (GHz)	Analytic (GHz)	Formula (GHz)	Measurement (GHz)
3	80	0.4	0.6	3.9	6	0.76121	0.64423	0.58998	0.68707
3	1	0.2	0.5	3.9	8	0.5133	0.4569	0.46844	0.51272
3	80	0.1	0.6	3.9	4	0.83717	0.6081	0.79274	0.8644
3	1	0.3	0.3	3.9	8	0.48207	0.4913	0.47303	0.478
3	80	0.2	0.6	3.9	8	0.33434	0.2943	0.32953	0.34733
3	50	0.2	0.6	3.9	4	1.066	0.8404	0.9385	1.027
3	50	0.1	0.5	3.9	6	0.47752	0.36	0.42399	0.4887
3	1	0.2	0.3	3.9	8	0.44919	0.4343	0.43161	0.45053
3	50	0.1	0.6	3.9	6	0.48742	0.36642	0.43656	0.499
3	80	0.2	0.6	3.9	6	0.5357	0.4379	0.50444	0.5284
3	50	0.3	0.5	3.9	4	1.3705	1.1177	0.99893	1.293
3	80	0.4	0.3	3.9	6	0.6159	0.58797	0.52794	0.60867
3	1	0.1	0.3	3.9	8	0.4234	0.383	0.36903	0.43181
3	50	0.2	0.5	3.9	8	0.32455	0.2951	0.32394	0.33813
3	50	0.3	0.5	3.9	8	0.36758	0.3382	0.35503	0.35587
3	50	0.4	0.3	3.9	8	0.35631	0.36424	0.34909	0.35333
3	1	0.3	0.5	3.9	4	2.004	1.6777	1.4445	2.0454
3	50	0.2	0.5	3.9	6	0.52859	0.4386	0.49589	0.51547
3	1	0.1	0.6	3.9	4	1.1576	0.95421	1.1603	1.2237
3	1	0.1	0.4	3.9	8	0.44747	0.392	0.38645	0.45717
3	80	0.3	0.5	3.9	4	1.2939	1.0895	0.98688	1.2825
3	50	0.1	0.5	3.9	8	0.3133	0.2529	0.27697	0.33687
3	50	0.1	0.6	3.9	4	0.86727	0.62246	0.80242	0.8733
3	50	0.1	0.3	3.9	6	0.44657	0.34077	0.39065	0.461
3	80	0.2	0.3	3.9	4	0.8899	0.74345	0.82967	0.9232
3	80	0.3	0.4	3.9	4	1.2482	1.056	0.95221	1.2415
3	1	0.3	0.5	3.9	6	0.8715	0.8011	0.7859	0.9025
3	1	0.2	0.5	3.9	6	0.7479	0.6716	0.71709	0.78022
3	50	0.1	0.6	3.9	8	0.32747	0.2571	0.28519	0.34573
3	80	0.3	0.3	3.9	4	1.1367	1.0144	0.90929	1.1827
3	50	0.1	0.4	3.9	8	0.31101	0.24753	0.26724	0.328
3	80	0.3	0.5	3.9	6	0.5884	0.5155	0.53692	0.5732
3	80	0.1	0.3	3.9	6	0.4387	0.33286	0.38594	0.46307
3	50	0.1	0.4	3.9	6	0.46556	0.3518	0.40909	0.48
3	50	0.3	0.4	3.9	6	0.55505	0.5134	0.52438	0.55473
3	1	0.4	0.6	3.9	6	1.1266	0.99461	0.86357	1.1374
3	50	0.3	0.5	3.9	6	0.6005	0.5287	0.54348	0.57373
3	1	0.3	0.6	3.9	4	2.1102	1.7177	1.4874	2.1372
3	1	0.3	0.6	3.9	8	0.57626	0.5282	0.52862	0.57944
3	80	0.4	0.4	3.9	8	0.3703	0.36813	0.36116	0.3716
3	80	0.2	0.4	3.9	6	0.48434	0.4159	0.47269	0.49947
3	50	0.3	0.3	3.9	4	1.1842	1.0412	0.9204	1.193
3	50	0.4	0.3	3.9	6	0.63121	0.60346	0.53439	0.61173
3	50	0.1	0.3	3.9	4	0.7685	0.5741	0.71803	0.7967
3	1	0.3	0.6	3.9	6	0.9214	0.8187	0.80921	0.94386
3	1	0.4	0.4	3.9	8	0.57152	0.57715	0.52863	0.5785
3	50	0.2	0.3	3.9	8	0.31202	0.2776	0.29847	0.3128
3	1	0.1	0.4	3.9	4	1.0774	0.9175	1.0873	1.1515
3	50	0.3	0.6	3.9	8	0.3917	0.3459	0.36556	0.36347
3	1	0.1	0.6	3.9	8	0.47979	0.40332	0.4124	0.48917
3	50	0.2	0.3	3.9	6	0.4769	0.41084	0.4569	0.47747
3	80	0.1	0.3	3.9	4	0.7471	0.5605	0.70937	0.79627
3	80	0.2	0.3	3.9	8	0.30455	0.2708	0.29487	0.31467
3	1	0.2	0.6	3.9	4	1.536	1.2667	1.3571	1.5685
3	80	0.1	0.4	3.9	8	0.3053	0.2419	0.26402	0.3296
3	1	0.3	0.5	3.9	8	0.56182	0.5179	0.5134	0.55892
3	1	0.1	0.5	3.9	4	1.098	0.9381	1.1269	1.1893
3	1	0.1	0.3	3.9	4	1.0455	0.8899	1.0383	1.0725
3	80	0.2	0.4	3.9	8	0.3209	0.28048	0.30879	0.32773
3	1	0.2	0.4	3.9	4	1.3848	1.2014	1.2717	1.4257



*diction* (Springer Science & Business Media, 2009).

- [18] S. Diamond and S. Boyd, CVXPY: A Python-embedded modeling language for convex optimization, *Journal of Machine Learning Research* **17**, 1 (2016).